Molecular Biology of the Cell
Vol. 16, 4967–4981, October 2005

Early Spindle Assembly in *Drosophila* Embryos: Role of a Force Balance Involving Cytoskeletal Dynamics and Nuclear Mechanics[D] [V]

E. N. Cytrynbaum,*†‡ P. Sommi,*‡ I. Brust-Mascher,* J. M. Scholey,*§‖ and A. Mogilner*‖¶

*Laboratory of Cell and Computational Biology, Center for Genetics and Development, University of California, Davis, Davis, CA 95616; †Department of Mathematics, University of British Columbia, Vancouver, British Columbia V6T 1Z2, Canada; and §Section of Molecular and Cell Biology and ¶Department of Mathematics, University of California–Davis, Davis, CA 95616

Submitted February 23, 2005; Revised June 10, 2005; Accepted July 21, 2005
Monitoring Editor: Ted Salmon

Mitotic spindle morphogenesis depends upon the action of microtubules (MTs), motors and the cell cortex. Previously, we proposed that cortical- and MT-based motors acting alone can coordinate early spindle assembly in *Drosophila* embryos. Here, we tested this model using microscopy of living embryos to analyze spindle pole separation, cortical reorganization, and nuclear dynamics in interphase–prophase of cycles 11–13. We observe that actin caps remain flat as they expand and that furrows do not ingress. As centrosomes separate, they follow a linear trajectory, maintaining a constant pole-to-furrow distance while the nucleus progressively deforms along the elongating pole–pole axis. These observations are incorporated into a model in which outward forces generated by zones of active cortical dynein are balanced by inward forces produced by nuclear elasticity and during cycle 13, by Ncd, which localizes to interpolar MTs. Thus, the force-balance driving early spindle morphogenesis depends upon MT-based motors acting in concert with the cortex and nucleus.

INTRODUCTION

Mitosis, the process by which chromosomes are segregated from "mother" to "daughter" cells, depends upon the action of the spindle, a self-organizing molecular machine assembled from microtubule (MT) arrays and multiple molecular motors (Scholey *et al*., 2003). Force and movement generation by motors and MT dynamics is crucial for spindle assembly and development (Inoue and Salmon, 1995; Sharp *et al*., 2000a; Nedelec 2002; Cytrynbaum *et al*., 2003), but the coordination between the mechanical elements of the spindle remains unclear. To elucidate the mechanisms of the coordinated movements and force balances in mitosis, we turned our attention to the rapid and simultaneous formation of thousands of spindles during early *Drosophila* embryogenesis, the well studied genetics and biochemistry of which make this system particularly convenient for investigating spindle development (Tram *et al*., 2001; Kwon and Scholey, 2004).

The *Drosophila* embryo is syncytial for the first 13 rapid cycles of mitosis. The nuclei, initially in the interior of the embryo, migrate to its surface, and syncytial blastoderm divisions (cycles 10–13) occur at the cortex of the embryo, just beneath the plasma membrane, where dramatic redistribution of the cortical actin accompanies spindle morphogenesis (Foe and Alberts, 1983; Foe *et al*., 2000). During interphase, nuclei are contained within "buds" of cortical cytoplasm, whereas actin concentrates into "caps" centered above each cortical nucleus and above the apically positioned centrosomes. As the nuclei progress into prophase, the centrosomes migrate toward opposite poles and the actin caps evolve into an oblong ring referred to as a pseudocleavage "furrow" (Sullivan and Theurkauf, 1995) that outlines each nucleus and its associated separated centrosome pair (Karr and Alberts, 1986; Kellogg *et al*., 1988; Foe *et al*., 2000). After nuclear envelope breakdown (NEB), the centrosomes (spindle poles) continue to separate, first in prometaphase–metaphase and then again in anaphase. The furrows meanwhile invaginate in metaphase, serving as barriers between adjacent spindles and regress during late anaphase and telophase.

Each centrosome nucleates a radial array of MTs oriented with their plus ends distal (Sullivan and Theurkauf, 1995). Some of these MTs are astral, extending outward to the cortex, and some are interpolar (ipMT), cross-linked into an antiparallel bundle. Nearly 30 years ago, McIntosh *et al*. (1969) suggested that the spindle poles could be separated by a sliding filament mechanism, in which force-generating enzymes cross-linking overlapping ipMTs slide them apart

This article was published online ahead of print in *MBC in Press* (http://www.molbiolcell.org/cgi/doi/10.1091/mbc.E05–02–0154) on August 3, 2005.

[D] [V] The online version of this article contains supplemental material at *MBC Online* (http://www.molbiolcell.org).

‡ These authors contributed equally to this work.

‖ These authors are codirectors of this project.

Address correspondence to: A. Mogilner (mogilner@math.ucdavis.edu).

Abbreviations used: ip, interpolar; MT, microtubule; NEB, nuclear envelope breakdown.

relative to one another (McIntosh *et al*., 1969). Biochemical and ultrastuctural data support this suggestion, providing evidence that the bipolar kinesin-5 KLP61F, a plus end-directed motor, acts by such a mechanism (Sharp *et al*., 1999a; Lawrence *et al*., 2004; Kapitein *et al*., 2005). There also exists evidence that the C-terminal kinesin-14 Ncd, a minus end-directed motor, can cross-link and presumably slide together adjacent MTs (McDonald *et al*., 1990; Karabay and Walker, 1999; Lawrence *et al*., 2004). It is also plausible that dynein anchored on the actin cortex can slide astral MTs apart (Dujardin and Vallee, 2002) and separate spindle poles. Actin dynamics must play an important role(s) in centrosome separation based on the observation that separation is incomplete in *Drosophila* embryos treated with cytochalasin D (Stevenson *et al*., 2001).

Using antibody injection and mutant experiments, we obtained data suggesting that a multiple transient steady state model can explain how these three MT sliding motors, together with MTs, cooperate in spindle pole separation (Sharp *et al*., 2000a; Cytrynbaum *et al*., 2003; Brust-Mascher *et al*., 2004). According to this model, in interphase–prophase, dynein pulls the astral MTs toward the cortex generating an outward force on the centrosomes, which is countered by the inward force developed by Ncd contracting the ipMT bundle. As the pole-to-pole separation increases, the growing inward force that is proportional to the ipMT overlap length and constant outward forces balance one another, and the spindle poles achieve a constant spacing. After NEB, this balance is tipped by KLP61F that is released from the nucleus and together with other motors contributes to the outward force by sliding the ipMTs apart to maintain and then increase the spacing of the spindle poles (Sharp *et al*., 1999b, 2000a).

The mechanical and regulation dynamics of the mitotic spindle is so complex and the number of essential molecular players is so great that the best strategy is to try to understand the simplest stages of spindle morphogenesis first. The reason we address spindle pole separation in interphase–prophase only is that, early in mitosis, most of the force-generating components that are active subsequent to NEB, including KLP61F, chromokinesins, and kinetochore motors, are sequestered in the nucleus and do not contribute to the process. The "first generation" quantitative model (Cytrynbaum *et al*., 2003) explained the quantitative experimental data reasonably well; however, it was based on so many simplifying assumptions and free parameters that rather than having predictive power, it merely identified areas of uncertainty in which further work would be required to test and refine the model.

In this article, we address experimentally existing uncertainties and propose the second generation of the model. First, the magnitude of the outward force depends on the localization and activity of dynein motors. We assumed that dynein colocalizes with the actin furrows, supported partially by data in Sharp *et al*. (2000a) but not with the apparently hollow actin caps in interphase–prophase. The latter part of this assumption was essential for if there was dynein activity in the cap, it could pull the centrosomes inward negating the outward force. Justification for this assumption came from the observation that phalloidin staining of fixed embryos showed actin either in caps early in prophase or in hollowed-out rings late in prophase (Foe *et al*., 2000). It has also been claimed that dynein localizes to the nucleus, playing a role in the anchoring of MTs and centrosomes to the nucleus as well as driving pre-NEB centrosome separation in *Drosophila* (Robinson *et al*., 1999). To differentiate between cortex- and nucleus-driven separation, we 1) used four-dimensional (4-D) quantitative microscopy (Marshall et al., 2001) to analyze dynamic actin redistribution and 2) studied dynein localization.

Second, we assumed that the centrosomes separate along the azimuth of a rigid spherical nucleus. To examine this assumption, we 3) used microscopy to analyze nuclear shape and centrosome trajectories.

Third, the model was based on the assumption that the inward force increases with pole-to-pole separation, which implies that the overlapping MT length, and not the number of Ncd motors is the corresponding limiting factor. To examine this assumption, we 4) studied the Ncd localization.

Fourth, the magnitude of the forces shaping the spindle has not been measured directly. We 5) used computational modeling to estimate the forces indirectly.

We found that 1) actin caps are not hollow and not static; they expand in synchrony with separating centrosomes; 2) actin furrows do not descend before NEB; 3) centrosomes separate along linear trajectories right under the actin cortex; 4) the nucleus deforms and aligns with the spindle axis; and 5) dynein colocalizes with the actin cortex, whereas Ncd colocalizes with ipMT bundles. These findings lead us to change some of the modeling assumptions, while providing justification for other ones. We suggest that the quantitative model successfully explains the data and that 1) dynein generates a constant outward force; 2) Ncd and nuclear elasticity cooperate in developing an inward spring-like force; 3) the balance of the effective drag, the dynein and nuclear elastic forces, and in cycle 13, the Ncd force, explains the kinetics of pole separation before NEB.

MATERIALS AND METHODS

Fly Stocks and Embryo Collection

Flies were maintained and embryos selected as described previously (Sharp *et al*. 1999b). Experiments were performed using green fluorescent protein (GFP)-tubulin (provided by Dr. Allan Spradling, Carnegie Institution of Washington, Washington, DC), GFP-Ncd (provided by Dr. Sharyn Endow, Duke University Medical Center, Durham, NC), GFP-Polo (provided by Dr. Claudio Sunkel, Universidade do Porto, Porto, Portugal) and Claret nondisjunctional (ca^{nd}) mutant embryos (provided by Dr. Scott Hawley, Stowers Institute for Medical Research, Kansas City, MO). Ncd null embryos were generated by crossing homozygous (ca^{nd}) females with heterozygous or homozygous (ca^{nd}) males.

Pole-to-Pole and Pole-to-Actin Furrow Spacing

GFP-tubulin embryos, NCD null embryos injected with rhodamine tubulin (Cytoskeleton, Denver, CO), or GFP-Polo embryos injected with rhodamine-actin (monomeric actin; Cytoskeleton) were used as indicated. Time-lapse confocal images were acquired on an Olympus (Melville, NY) microscope equipped with an Ultra View spinning disk confocal head (PerkinElmer Life and Analytical Sciences, Boston, MA). Images were analyzed using MetaMorph Imaging software (Universal Imaging, Downingtown, PA) and custom-written software using Matlab (Mathworks, Natick, MA). To measure the pole-to-actin furrow distance, GFP-Polo and rhodamine-actin images were merged. Pole-to-pole distance was calculated by drawing a straight line connecting paired poles; pole-to-furrow distances were calculated by drawing straight lines connecting the inner face of the actin furrow and the corresponding closest pole in the directions along and perpendicular to the spindle long axis. The long axis was determined by the pole-to-pole direction. Alexa Fluor 647 Phalloidin (Molecular Probes, Eugene, OR) was used in combination with rhodamine-actin (Cytoskeleton). The depths of the actin furrows and centrosomes were calculated using stacks of images at 0.5-μm spacing.

Immunofluorescence Microscopy

Fixation of *Drosophila* embryos for immunofluorescence was performed as described previously (Sharp *et al*. 1999b). Triple labeling was performed with mouse anti-dynein (Sharp *et al*. 2000a,b) and goat anti-actin-rhodamine-conjugated (Santa Cruz Biotechnology, Santa Cruz, CA) and rabbit anti-tubulin (Sharp et al. 2000a) antibodies. The appropriate secondary antibody (Jackson ImmunoResearch Laboratories, West Grove, PA) was used.

Measurements of Nuclear Deformation

To measure nuclear deformation, GFP-Polo embryos were injected with rhodamine-dextran 70 kDa (Molecular Probe) and stacks of images at 0.5-μm spacing were taken over time. The 70-kDa dextran is excluded from the nucleus, thus providing a nuclear outline marker. The outer edge of each nucleus was fitted with an ellipse (least-squares fit to a manually selected set of points) that gave a measure of the extent of deformation (the ratio of the major axis to the minor axis) and the direction of maximal deformation (the angle of the major axis) relative to the spindle axis. Nucleus size was measured in a similar manner.

Statistical Analysis of the Nucleus Deformation, Average Tubulin Distribution, and Separation Time-Course Data

Partitioning the separation distances into bins allowed for comparison of the distribution of angles between the nuclear and spindle axes in each bin to the uniform distribution − the expected distribution if the two axes were completely uncorrelated. Kolmogorov-Smirnov (KS) tests were performed on each bin (a p value of $p < 0.05$ is interpreted to mean that the distribution of angles for that bin is not uniform). Statistical analyses of the tubulin distributions were done using Excel and Matlab routines. Custom Matlab scripts were used to calculate the average tubulin images by digitally extracting and rotating each bud, compiling aligned buds by centrosome separation and averaging the aligned images pixelwise. Comparison of steady state and characteristic times of separation for wild-type (wt) and Ncd null embryos was done using KS tests to determine differences in distributions that were measured by fitting each individual separation curve with a simple logistic model.

Mathematical Modeling

Force–Velocity Relationships. For dynein, Ncd, and "polymerization" motors, we assumed linear force–velocity relationships: $F = F_{stall}(1 - [v/v_{free}])$. Here, F is the force the motor generates if moving with velocity v, F_{stall} is the stall force, and v_{free} is the rate of movement of the unloaded motor. Such a force–velocity relationship is a good approximation to the data for dynein and polymerization force (Dogterom and Yurke 1997; Hirakawa *et al*., 2000); we assume the same is true for Ncd (see more detailed discussion in Cytrynbaum *et al*., 2003; Brust-Mascher *et al*., 2004).

Nuclear Elastic Force. We assume the nucleus can be modeled by a network of three springs, one attached by a free hinge to each centrosome and a third spring positioned vertically so as to push against the cortex, generating force only under compression (Figure S1A). At a given value of the centrosome separation, S, two equations—one for a vertical force balance at the hinge and one for a horizontal balance at the centrosomes—lead to the following equation:

$$3s^2 - 4sy + (1 - 3s^2)y^2 + 4sy^3 - \frac{4}{3}y^4 = 0,$$

where $s = S/D$, $F_{\mathrm{nucl}}(S) = k(S - Y(S))$, and $y = Y(S)/D$. Here, k is the spring constant, and D is the nuclear diameter. The rest length of each spring is $D/2$. Numerical solution of this equation gives the nuclear elastic force as a function of S (Figure S1B). At small separation, $S \ll D$, $Y(S) \approx S - (S^3/6D^2)$ and this force is very small, $F_{nucl}(S) \approx kS^3/6D^2$, whereas at large separation, $S > D$, $Y(S) \approx D$ and the force is linearly proportional to the separation $F_{nucl}(S) \approx k(S - D)$. We use the last expression to find the stationary separation (Eq. 2) and time constant (Eq. 3).

To estimate the spring constant, we use the measured nuclear Young's modulus $E \sim 20$ pN/μm (Tseng *et al*., 2004). Then, $k \sim ED \sim 100$ pN/μm. Indirectly, other data also support this estimate. Dahl *et al*. (2004) report a value for the tension (originating from deformed nuclear envelope) caused by aspiration of a large nucleus ~25 mN/m ~ 25,000 pN/μm. For a nucleus ~250 μm in diameter, this tension would correspond to an effective Young's modulus ~100 pN/μm, which is the same order of magnitude as the value we use. Houchmandzadeh *et al*. (1997) and Marshall *et al*. (2001) report the chromosome's Young's modulus of the order of hundreds to thousands piconewtons per micrometer. The effective nuclear elasticity is likely to be an order of magnitude less than that of the chromosome, because when the nucleus is deformed, the chromosomes can shift relative to each other. This argument also supports the order of magnitude estimate that we use.

Theoretical Fitting of the Data. We used the Matlab ODE solver to verify that the numerical solution of Eq. 1 can be approximated very well with the equation $S(t)\ S_{st}/(1 + \exp[-(t - \ddot{o})/\hat{o}])$. We used the Matlab least square routine to find the corresponding parameters S, $\hat{o}$, $\ddot{o}$ that give the best fit to the time series for the pole separation using this equation.

Computational Modeling

MT Dynamics. Individual MTs were nucleated randomly at a constant rate and anchored at the centrosome by their minus ends. Dynamic instability was modeled as a first order process as proposed by Dogterom and Leibler (1993), whereby each MT can be in either a growing or shrinking state with exponentially distributed transitions between the two states. On average, 100 MTs emanated from each centrosome. The average MT length was adjusted so that a few tens of MTs reached the cortex. The dynamic instability rates were at least a few fold faster than the centrosome movement rates. MTs whose plus ends are at the cortex formally remain in the growing state until a transition occur, even though their growth may cease as dictated by the force–velocity relationship for a growing MT. While at the cortex, they may attach and detach from active dynein motors until they undergo catastrophe and shrink away from the cortex. While attached to dynein, MTs are pulled on in accordance with the motors force–velocity relationship. While unattached, they generate a force in accordance with the polymerization force–velocity relationship (the MT plus end moves relative to the cortex as the centrosome to which it is anchored moves).

Actin and Dynein Regulation. We modeled mathematically the distribution of the diffusing kinases; motor mediated transport of the kinases along the astral MTs call for more complex equations that give qualitatively similar solutions. The distribution of the kinases around the centrosome satisfies similar diffusion–reaction equations, the quasi-steady-state solutions at location $\vec{x}$ along the cortex being

$$.kin_{a,d}(\vec{x}) = kin^0_{a,d}\left[\frac{\exp(-\sqrt{\lambda_{a,d}/D_{a,d}}|\vec{x} - \vec{c}_1|)}{|\vec{x} - \vec{c}_1|} + \frac{\exp(-\sqrt{\lambda_{a,d}/D_{a,d}}|\vec{x} - \vec{c}_2|)}{|\vec{x} - \vec{c}_2|}\right]$$

Here, indices a,d relate to kinases that regulate actin and dynein, respectively. The diffusion coefficient is $D_{a,d}$, $\lambda_{a,d}$ is the rate at which the kinase is dephosphorylated (assumed to be uniform in space), and $\vec{c}_{1,2}$ are the positions of the centrosomes. At the cortex, we assume that dynein is down-regulated by the kinase according to Michaelis-Menten kinetics leading to a distribution of active dynein given by $Dyn(\vec{x}) = Dyn_0\{\delta^r/(\delta^r + kin_d[\vec{x}]^r)\}$. The probability of an MT attaching to active dynein at the cortex is then proportional to $Dyn(\vec{x})$, illustrated in Figure 10D. The actual force exerted by active dynein, illustrated in Figure 10B, is proportional to the product of $Dyn(\vec{x})$, F-actin density at the cortex $a(\vec{x}, t)$, and the local MT density (see Table S1 for definition of terms).

We assume that the second kinase affects the local actin polymerization rate $p(\vec{x})$ according to the following Michaelis-Menten process: $p(\vec{x}) = p_0\{kin_a(\vec{x})^m/(\alpha^m + kin_a[\vec{x}]^m)\}$.

We describe the F-actin dynamics at the cortex with the following simple model: $\partial a/\partial t = p(\vec{x})\ a\ (1 - a) - \gamma_1 a + \gamma_2$, where $a(\vec{x}, t)$ is the F-actin density at the cortex, γ_1 is the actin depolymerization rate, and γ_2 is the background polymerization rate. We are normalizing the maximal actin density to 1 and assuming that the polymerization rate decreases when the density is close to maximal (due to self-limiting dynamics). When the kinase and actin dynamics are fast compared with centrosome movement, the density of actin filaments at the cortex is given by the following formula:

$$a \approx \frac{1}{2} - \frac{\gamma_1}{2p(\vec{x})} + \frac{1}{2}\sqrt{\left(1 - \frac{\gamma_1}{p(\vec{x})}\right)^2 + 4\frac{\gamma_2}{p(\vec{x})}}$$

The corresponding computed F-actin density is illustrated with the shading of the "cortex bar" in Figure 10B. Note that all parameters specific to the computational model are given in Table S1.

Cross-linking To determine whether two MTs from the opposite poles will be cross-linked by Ncd motors, we track the angle between them. If the cosine of this angle is sufficiently small (or equivalently, if the angle between them is sufficiently large), the MTs are cross-linked. We find that when the angle-threshold for cross-linking is ≈120° or larger, separation is not reliable. For less restrictive cross-linking, MT depletion at the cortex is sufficient to robustly generate the required asymmetry of cortical forces on the centrosomes (Figure 10C).

Ncd Forces. Once MTs are cross-linked, they continue to undergo dynamic instability. Ncd motors are assumed to bind in the overlap region at a constant number of motors per micron, under the assumption that antiparallel overlap is the rate limiting quantity in Ncd force generation.

Force Balance Equations. Figure S1 shows an instance of each of the types of forces and velocities (with notation) that are included in the following equations:

$$\sum_{dyn1} F_d\left(1 - \frac{\vec{v}_1 \bullet \vec{u}_{dyn1}}{v_d}\right)\vec{u}_{dyn1} - \sum_{pol1} F_{pol}\left(1 + \frac{\vec{v}_1 \bullet \vec{u}_{pol1}}{v_p}\right)\vec{u}_{pol1} +$$

$$\rho_{ncd}O_{ipMT}F_{ncd}\left(1 + \frac{(\vec{v}_2 - \vec{v}_1)\bullet\vec{u}_N}{v_n}\right)\vec{u}_N - k(R_1 - R_0)\vec{u}_{n1} - \mu_c\vec{v}_1 = 0$$

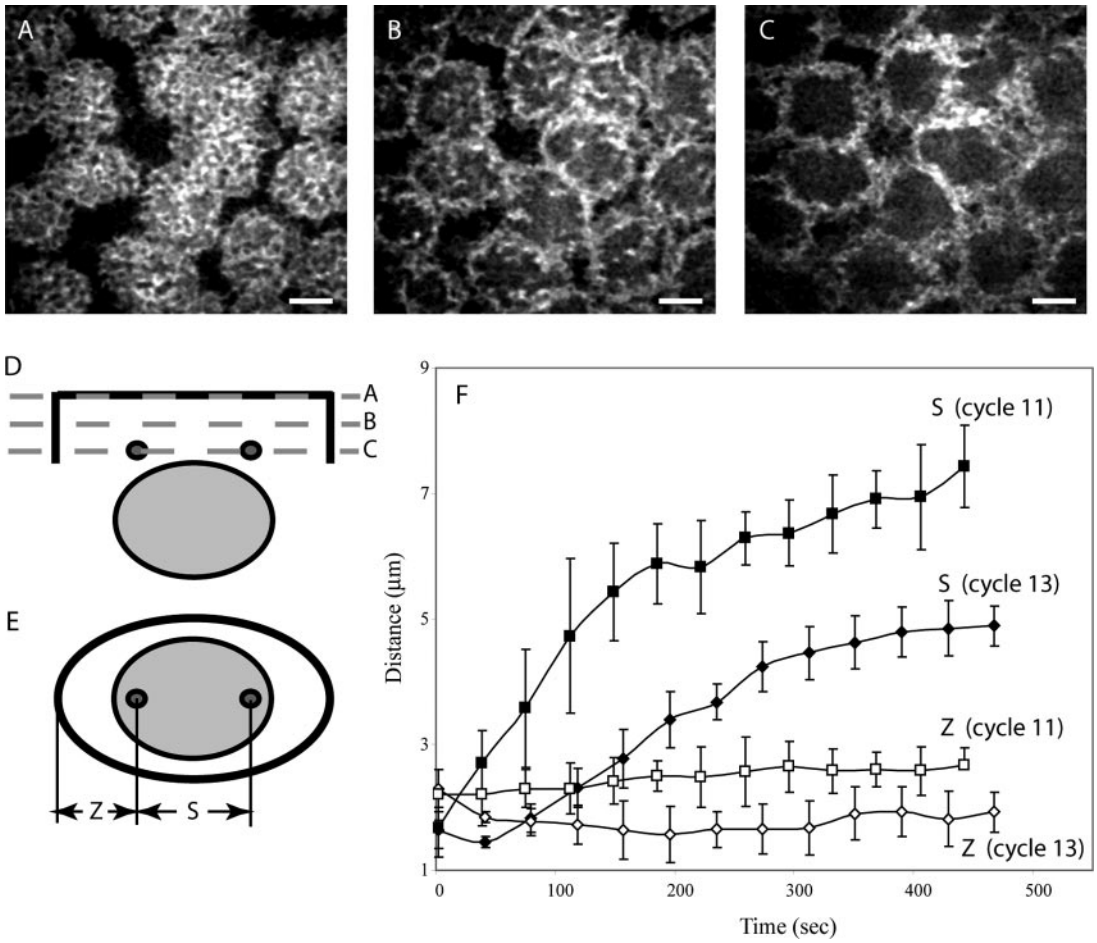

Figure 1. Four-dimensional microscopy of a GFP-Polo-expressing embryo injected with rhodamine-actin. (A–C) Actin distribution in three consecutive confocal planes: at the cortex (A), 1 μm below the cortex (B), and 2 μm below the cortex (C). (D and E) Suggested geometry of the actin caps (plane A) and furrow (planes B and C) in relation to the position of the nucleus and centrosomes, shown in cross section, (D), and parallel to the cortex (E). (F) Pole-to-pole (*S*) and pole-to-furrow (*Z*) distances as functions of time in cycles 11 and 13. Bar, 5 μm.

$$\sum_{dyn2} F_d\left(1-\frac{\vec{v}_2\bullet\vec{u}_{dyn2}}{v_d}\right)\vec{u}_{dyn2}-\sum_{pol2} F_{pol}\left(1+\frac{\vec{v}_2\bullet\vec{u}_{pol2}}{v_p}\right)\vec{u}_{pol2}-$$

$$\rho_{ncd}O_{ipMT}F_{ncd}\left(1+\frac{(\vec{v}_2-\vec{v}_1)\bullet\vec{u}_N}{v_n}\right)\vec{u}_N-k(R_2-R_0)\vec{u}_{n2}-\mu_c\vec{v}_2=0$$

$$k(R_1-R_0)\vec{u}_{n1}+k(R_2-R_0)\vec{u}_{n2}-k(R_0-N_y)H(R_0-N_y)\vec{y}-\mu_n\vec{v}_N=0$$

Here, the first two equations describe the balance of forces acting on the two centrosomes, and the third equation describes the forces acting on the nucleus. Each of the *dyn* summations is over all the MTs that are attached to the cortex and each of the *pol* summations is over all the unattached and polymerizing MTs at the cortex. R_0 is the radius of the undeformed nucleus, and R_1 and R_2 measure the current distance between the center of the nucleus and each centrosome. μ_c and μ_n are the drag coefficients for the centrosomes and nucleus, respectively, and $\vec{v}_1$, $\vec{v}_2$, and $\vec{v}_3$ are the velocities of the centrosomes and nucleus, respectively. O_{ipMT} is the dynamically changing cross-linked MT overlap length, and H is the Heaviside function. Note that these three vector equations contain six scalar equations, and there are six unknowns to be calculated: the *x*- and *y*-components of the velocities of each centrosome and the nucleus. We use a custom Matlab code to solve the algebraic force balance and actin dynamic equations, to update the MT configuration at each computational step, and to move the centrosomes, MT asters, and nucleus using a Forward Euler method.

Online Supplemental Material

Figure S1 is a model of the nuclear elastic forces. Table S1 provides model parameters. The videos show (Video 1) time-lapse movie of GFP-tubulin expressing embryo injected with rodamine-actin; actin dynamics of a single "bud" during interphase-prophase (Video 2), simulation of the MT cross linking mechanism for generating cortical force asymmetry (only astral MTs are shown) (Video 3), and simulation of the dynein regulation mechanism for generating asymmetry (Video 4).

RESULTS

Expansion of "Solid" and Flat Actin Caps Accompanies Spindle Pole Separation; Actin Furrows Do Not Descend during Interphase–Prophase

As the centrosomes separate and begin to build the mitotic spindle, cortical actin undergoes gradual but distinctive changes in its distribution (Videos 1 and 2; Figure 1). During interphase, early in centrosome separation, cortical actin collects into a cap directly above each centrosome pair, and as separation proceeds, the cap expands (Figures 1F and 2A). Microinjection of fluorescently labeled actin allowed visualization of actin redistribution in vivo. We observed the presence of a solid actin cap throughout interphase–prophase (Figures 1 and 2), in contrast with the hollowing out of actin described by Foe *et al*. (2000). To understand the differences between the phalloidin staining in fixed embryos (Foe *et al*., 2000) and the labeled actin localization in live embryos, live embryos were simultaneously injected with actin and phalloidin. Remarkably, the phalloidin staining

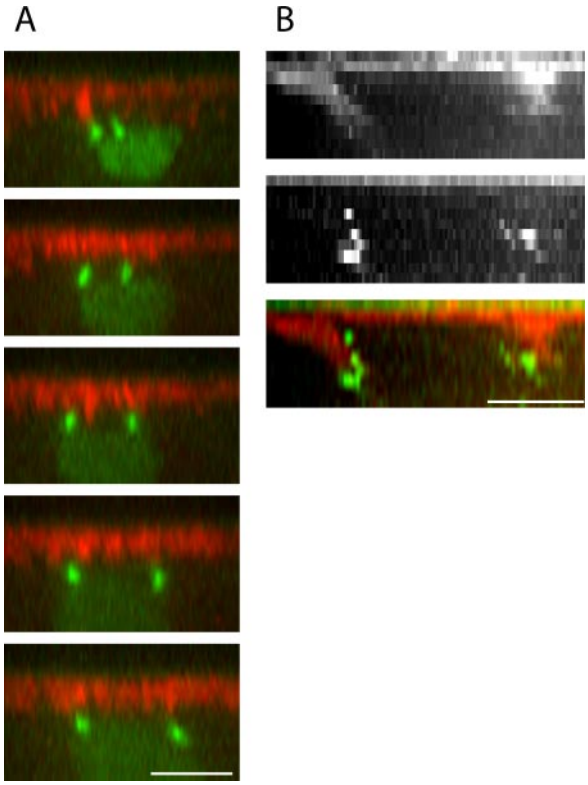

Figure 2. (A) Sequence of five cross sections from a time-lapse movie (37 s apart) showing actin and centrosomes (GFP-Polo-expressing embryo injected with rhodamine-actin). Note that throughout prophase, the flat actin cap is present with no evidence of hollowing out. (B) Simultaneous injection of rhodamine actin (top, red in merged) and Alexa phalloidin (middle, green in merged) into live embryos demonstrates their different localizations. Phalloidin marks the tips of the actin furrows (staining at the top is not specific), whereas rhodamine actin shows a broader distribution, including the complete furrows and caps. Bar, 5 μm.

was consistent with the observations of Foe *et al*. (2000), but the actin signal revealed the persistence of complete actin caps (Figure 2B). The difference between the two signals most likely indicates a difference in the structure and/or dynamics of the caps and furrows. One possible explanation stems from the observations of Nishida *et al*. (1987) who showed that cofilin competes with phalloidin when binding to filamentous actin. We present no evidence that cofilin is competing with phalloidin in this instance, but the Nishida *et al*. (1987) result raises the possibility that phalloidin might only be binding to a subpopulation of the F-actin present in the embryo based on a particular F-actin structure or a localized binding partner of actin. Another possibility is that the cap is formed of G-actin rather than F-actin. Although this is possible, it does not seem likely because G-actin is free to diffuse and would not remain in high concentrations at the cortex throughout mitosis (minutes), as observed.

We observed that the actin caps remained flat and that their depth was relatively constant throughout interphase–prophase (2 $\pm$ 0.7 μm; Figures 1 and 2A). Significantly, the actin furrows did not descend before NEB, maintaining a constant depth of ~2 μm throughout prophase (our unpublished data). In our study, we often observed "patches" of actin originating from the cortex and descending close to the centrosomes (Figure 2). When actin distribution was observed in consecutive focal planes, these actin patches were clearly visible below the cortex as protrusions of actin forming an intermediate zone between the dense actin cap and the plane where actin furrows start being visible (Figure 1B). Actin patches were always localized above and in proximity (~1–2 μm) to the centrosomes throughout the entire cycle, from interphase–prophase to anaphase (our unpublished data). Using three-dimensional images stacks, on many occasions we were able to notice localized hollowing of actin at the cortex in coincidence with these actin patches, suggesting a strong interaction between actin at the cortex and MTs reaching and deforming it.

The actin distribution relative to the centrosomes was measured in live embryos in an attempt to characterize the dynamic relationship between the two (Figures 1 and 2). Actin structures (cap and furrows) surround the centrosomes at a uniform distance throughout mitosis. The distances from the centrosomes to the furrows (along the centrosomal axis, *Z*; Figure 1F) were in the 2-μm range, and these distances were maintained throughout the entire cycle (Figure 1F). The centrosomal (long) axis of the actin cap/furrow structure elongates precisely with the centrosomes but the transverse axis does not elongate (our unpublished data). Precise measurements are given in Table 1.

This apparent regulation of the distance between the growing edge of the actin cap and the centrosomes raises the question of the pathway that couples them. To determine whether this constant distance was due to a coincidental or a causal mechanism, we carried out the same measurements in Ncd null embryos. The centrosomes have been reported to separate faster and to a larger extent in these embryos (Sharp *et al*. 2000a; Cytrynbaum *et al*., 2003); this provides a good test of the hypothesis that actin cap expansion is coupled to centrosome separation. We found that throughout cycles 11, 12, and 13, pole-to-furrow distances are indistinguishable when comparing wild type to Ncd null (Figure 3B and Table 1). Our measurements of cycle 13 separation rates and steady states indicate that wild-type and Ncd separation

Table 1. Cycle dependence of spatial and temporal scales of the spindle dynamics

	Prophase steady state (μm)		Time constant of the pole separation (s)		Nuclear diameter (μm)	Pole-to-furrow distance (μm)	
	Wild type	Ncd null	Wild type	Ncd null		Wild type	Ncd null
Cycle	(No. of spindles; no. of embryos)				(No of nuclei; no. of embryos)	(No. of nuclei)	
11	8.3 $\pm$ 0.4 (10; 1)	8.2 $\pm$ 0.7 (18; 2)	65.6 $\pm$ 25.5 (10; 1)	60.0 $\pm$ 30.2 (18; 2)	5.5 $\pm$ 0.5 (98; 4)	2.4 $\pm$ 0.9 (938)	2.4 $\pm$ 0.7 (256)
12	7.1 $\pm$ 0.6 (25; 2)	7.1 $\pm$ 0.7 (15; 2)	69.6 $\pm$ 19.1 (25; 2)	78.4 $\pm$ 35.5 (15; 2)	5.0 $\pm$ 0.8 (174; 3)	2.6 $\pm$ 0.7 (928)	2.7 $\pm$ 0.6 (540)
13	4.7 $\pm$ 0.6 (53; 2)	6.0 $\pm$ 0.7 (48; 4)	115.7 $\pm$ 29.7 (53; 2)	89.9 $\pm$ 33.6 (48; 4)	4.5 $\pm$ 0.6 (218; 4)	1.9 $\pm$ 0.6 (733)	1.7 $\pm$ 0.5 (1070)

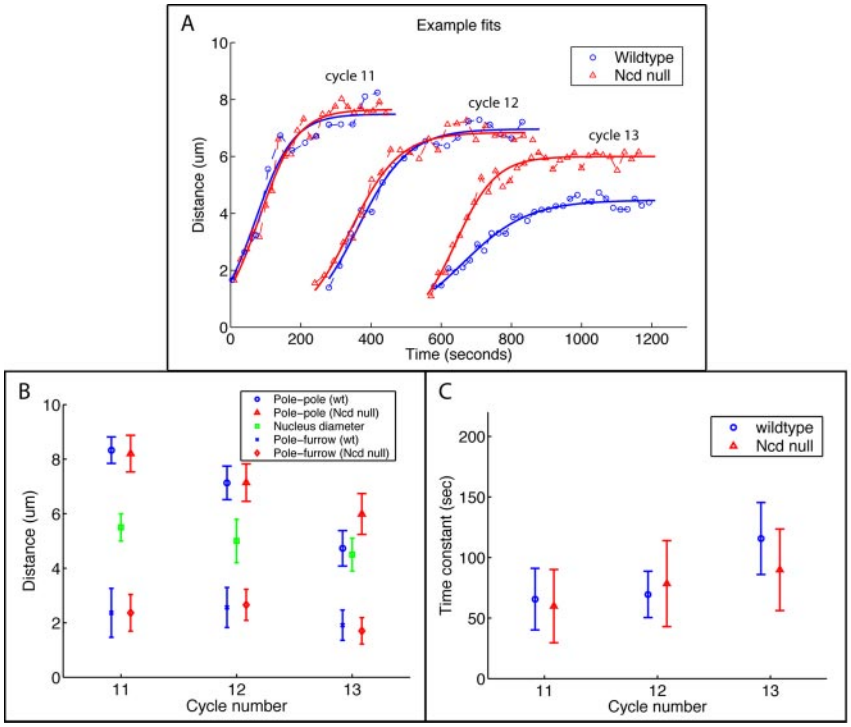

Figure 3. (A) Pole-to-pole distance in cycles 11–13 as a function of time in wild-type (blue, circles) and Ncd null (red, triangles) embryos. The curves are theoretical fits to the experimental data used to estimate the time constant and steady state of separation. (B) Steady state pole–pole separation in wild-type (blue circle) and Ncd null (red triangle) embryos, constant pole–furrow distance in wild-type (blue cross) and Ncd null (red diamond) embryos, and nuclear diameter (green square) in cycles 11–13. (C) Time constant of spindle elongation in wild-type (blue circle) and Ncd null (red triangle) embryos in cycles 11–13.

rates differ by ~28% (Figures 3, B and C), whereas the pole-to-furrow measurements indicate that the pole-to-furrow distance remains constant in time in both wild-type and Ncd null embryos and that this constant distance is the same in both embryo types.

Measurement of the Separation Time Course during Cycles 11, 12, and 13 Reveals Cycle Dependence in the Ncd Null Phenotype

We measured the pole-to-pole distance as a function of time in three consecutive cycles in both wild-type and Ncd null embryos (Figures 1F and 2 and Table 1) and confirmed that the separation kinetics are hyperbolic-like: the separation rate is maximal in the beginning, slowing down gradually as the separation approaches the transient prophase steady state (Figures 1F and 3A).

In both wild-type and Ncd null embryos, the steady maximal pre-NEB spindle length decreases in each subsequent cycle (Table 1 and Figure 3B), and this decrease is accompanied by a comparable decrease in the average nuclear size, although the decrease in wild-type cycle 13 is disproportionately large (Table 1 and Figure 3B). Notably, there is no difference between wild-type and Ncd null steady states in either cycle 11 or cycle 12, but in cycle 13 the wild-type steady state is significantly smaller (Table 1 and Figure 3B).

The characteristic times of separation in both embryo types in cycles 11 and 12 are all statistically indistinguishable. The Ncd null characteristic times are indistinguishable from each other in all three cycles. Again in sharp contrast, the wild-type cycle 13 characteristic time is significantly different from all others in both embryo types (Table 1 and Figure 3C).

Although large variations in the Ncd null data may account for some of the lack of distinction between distributions, it is clear that wild-type cycle 13 is anomalous in both its steady state and characteristic time of separation. As quantified below with the aid of the mathematical model, these results imply that Ncd does not play a role in the balance of forces in interphase–prophase of cycles 11 and 12 but does make an impact in cycle 13. Thus, the effects of loss of Ncd function reported previously are specific to cycle 13 (Sharp *et al*. 2000a).

Dynein Colocalizes with Cortical Actin; Ncd Colocalizes with ipMT Bundles

To investigate the distribution of dynein and Ncd, we examined their localization in live and fixed embryos. In fixed embryos, dynein was found to colocalize with actin at the cortex throughout actin cap expansion: Figure 4 illustrates the colocalization of actin and dynein during interphase–early prophase, late prophase, and telophase.

GFP-Ncd-expressing embryos microinjected with rhodamine-tubulin clearly showed in vivo colocalization of Ncd with ipMT bundles that extend between the centrosomes before NEB (Figure 5). Although the GFP–Ncd localization confirms the presence of Ncd motors in the interpolar bundles, it is not clear whether Ncd is necessary for the formation of the bundles. We examined wild-type and Ncd null embryos for the prevalence of the bundles and found that bundles were more generally evident in wild-type than in Ncd null embryos. However, the image quality was not consistent enough to rule out the possibility that bundles in Ncd null embryos were present but simply not visible. Moreover, we observed that some wild-type embryos also failed to demonstrate bundling. Note that these early bundles are much smaller than those seen later in mitosis. Interestingly, despite the apparently negligible role played by Ncd in separation during cycle 12 (described above), Ncd localizes to the ipMT bundles in cycle 12 (Figure 5B), indicating that the cycle 13-specific role of Ncd in force generation is independent of its ability to localize to the bundles.

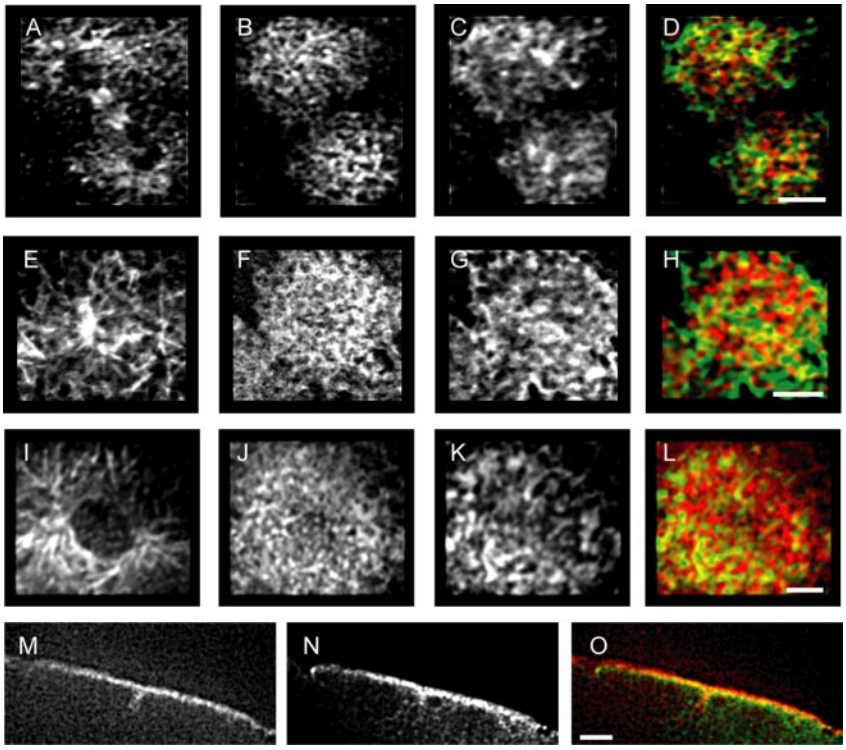

Figure 4. Actin (B, F, and J) and dynein (C, G, and K) distribution at the cortex in fixed embryos during telophase (A–D); interphase/early prophase (E–H), and late prophase (I–L). Areas of colocalization throughout the actin cap expansion between actin (red) and dynein (green) are visible in yellow in the merged images (D, H, and L). Tubulin (A, E, and I) shows MT distribution below the cortex. (M–O) Cross-sectional view shows actin (M) and dynein (N) colocalize at the cortex and furrows (O) during prophase. Bars, 5 μm.

Separating Centrosomes Follow Linear Trajectories during Interphase–Prophase

Surprisingly, three-dimensional tracking of centrosome trajectories showed deviation from what has been implicitly assumed in previous studies (Robinson *et al*., 1999; Sharp *et al*. 2000a; Cytrynbaum *et al*., 2003). Injection of GFP-polo embryos with both rhodamine-actin and dextran shows that centrosomes begin at the top of the nucleus ~2 μm below the cortex and separate in a roughly linear manner, remaining approximately the same distance from the cortex throughout separation (2 ± 0.7 μm) and without a significant vertical displacement of the nucleus (Figure 6). This indicates that either the centrosomes are not tightly anchored to the nucleus or the nucleus is not a completely rigid structure relative to the forces involved in centrosome separation. However, the centrosomes seem to be in close contact with the nucleus (Figure 6) throughout the period of spindle pole separation. Their exact distance from the nuclear surface is hard to estimate due to the amorphous structure of the centrosomes, so it is possible (in accordance with Figure 6) that this distance increases just a little (by ~1 μm) by late prophase, but the more significant factor is that the nucleus is not a rigid body and that it can be deformed under the influence of forces typical of those generated during spindle morphogenesis. Note that the centrosome trajectories are linear relative to the cortex (i.e., with respect to depth). The nature of the centrosomes' trajectory parallel to the cortex proved difficult to establish in a quantitative manner due to a lack of a fixed reference frame (drift and deformation of the nucleus as well as drift and dynamic turnover of the actin cortex with respect to the lab frame). Nevertheless, a comparison of these three structures (nucleus, actin cortex, and centrosomes) gives the impression that the centrosomes follow a roughly linear trajectory relative to the surrounding actin bud, whereas the nucleus is maneuvered into alignment with the surrounding actin bud and the centrosomes, as one might expect of a misaligned elastic body under tension from two points on its surface.

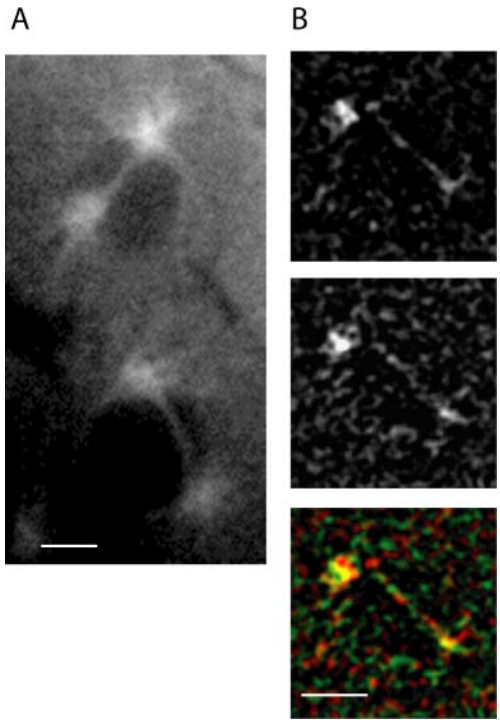

Figure 5. (A) Micrograph of a GFP-tubulin-expressing embryo shows two adjacent nuclei with ipMT bundles and centrosomes. Nuclear diameter is 5.5 ± 0.5 μm. (B) Ncd (top, red in merged) and tubulin (middle, green in merged) colocalize in ipMT bundles. Bar, 2.5 μm.

Another repercussion of the nondescending centrosome trajectory is that the net force acting on the centrosomes must be roughly parallel to the cortical surface. Further-

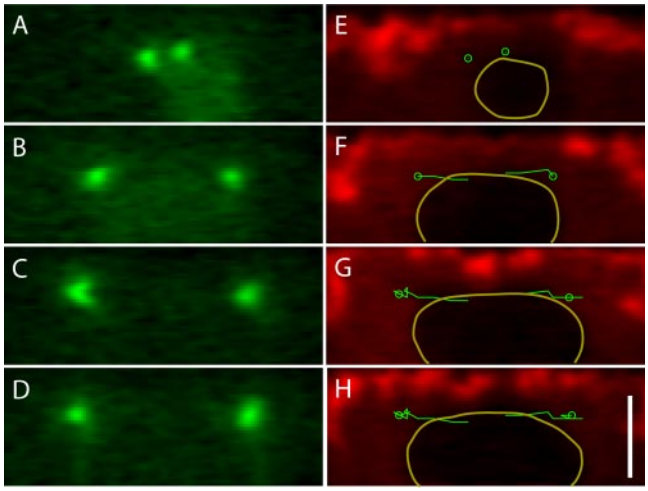

Figure 6. Centrosomes separate along linear trajectories right under the cortex, whereas the nucleus deforms. Four frames from a reconstructed cross section of a time-lapse confocal stack (t = 0 s [A], 167 s [B], 503 s [C], and 615 s [D]) showing GFP-polo (A–D) and rhodamine-dextrans (E–H) with the positions of the centrosomes (green circles) and centrosome trajectories (green line) overlaid. The contour of the nucleus is outlined in E–H. Note that the apparent increase in the size of the nucleus is mostly due to the fact that the centrosomes and nucleus do not start off perfectly aligned so that a cross section of the stack through the centrosome at the beginning of separation cuts through the nucleus off-center. Bar, 5 μm.

more, fixed cell immunofluorescence shows dynein colocalized with actin at the cortex and no significant signal elsewhere (Figure 4). We find no evidence to support nuclear localization of dynein in *Drosophila* syncytial blastoderm and would argue that the linear centrosome trajectories indicate that the cortex, rather than the nucleus, is providing the scaffolding for centrosome separation.

Examination of trajectories of individual pairs of centrosomes revealed that separation is not symmetric with respect to the nucleus. In some cases, one centrosome is completely static, whereas the other centrosome moves rapidly along the cortex, although as the centrosomes approach the pre-NEB steady state, this asymmetry relative to the nucleus disappears, likely due to the equilibration of elastic forces exerted by the nucleus.

The Nucleus Deforms and Aligns with the Pole-to-Pole Axis

The observation that the centrosomes separate just below the cortex in a roughly linear manner challenges the assumption that the nucleus is a relatively rigid sphere on whose surface the centrosomes migrate. To test the hypothesis that the nucleus is in fact deformable under forces typical of spindle morphogenesis, we took advantage of the fact that large dextrans are excluded from the nucleus, and using images of dextran-injected embryos, we were able to fit an ellipse to the outer edge of each nucleus. This provided a measure of the extent of deformation (the ratio of the major axis to the minor axis) and the direction of maximal deformation (the angle of the major axis) relative to the centrosomal axis. Figure 7, A–C, shows an example of this measurement technique.

It was difficult to resolve the shape of the nucleus in the confocal planes containing the centrosomes, where maximal deformations would be expected, due to cortical artifacts

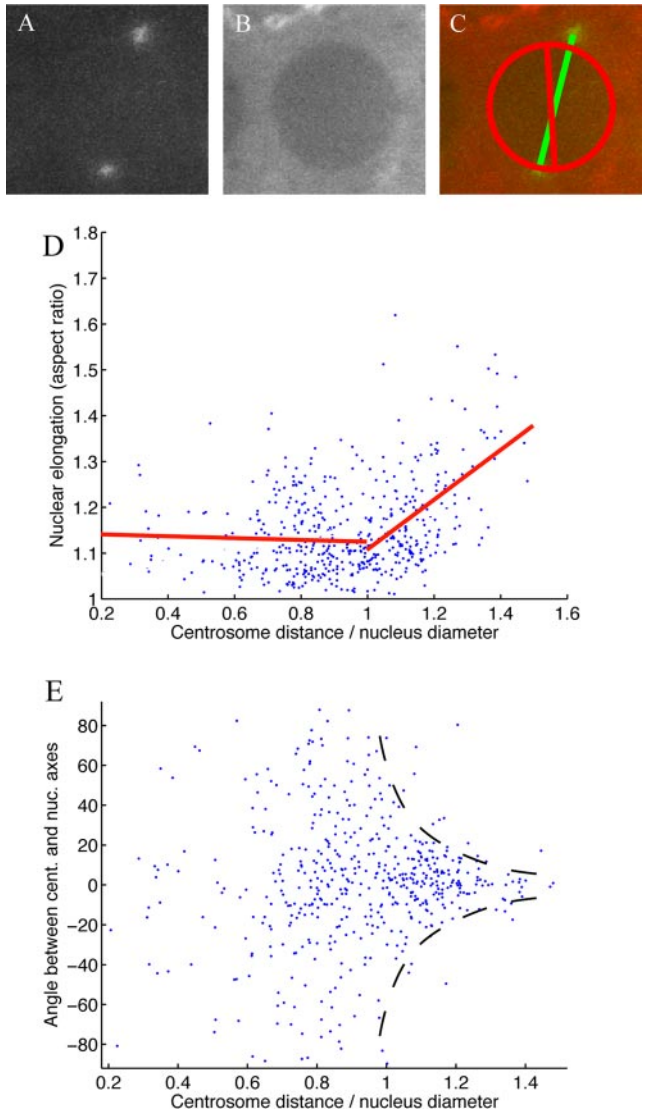

Figure 7. Nuclear deformation and alignment with spindle axis. GFP-polo image showing centrosomes (A), rhodamine-dextrans showing nuclear outline (B), and merged image (C) with an ellipse fit to the nuclear outline and the ellipse's major axis (red) and spindle axis (green) superimposed to demonstrate the measurement technique. (D) Scatter plot of nuclear elongation (the ratio of major to minor axes) as a function of pole-to-pole distance. For separation distances less than the nuclear diameter, elongation is minor and uncorrelated with pole-to-pole distance (slope m = −0.02), but as centrosomes extend beyond the nucleus' perimeter, nuclear elongation increases with separation (slope m = 0.5). (E) Scatter plot of the angles between the spindle axis and the major axis of the ellipse (i.e., long axis of the nucleus) as a function of pole-to-pole distance. Note that when the centrosomes are close, the angles range widely but as the centrosomes reach opposite sides of the nucleus, the angle distribution narrows around zero.

(dextrans seem to colocalize with actin), so we looked for deformations at 2–4 μm below the centrosomes where deformations might be smaller but could be resolved. To test the hypothesis that the forces applied to the centrosomes deform the nucleus, we measured both the extent of nuclear elongation (Figure 7D) and the angle between the centrosomal axis and the axis of measured elongation (Figure 7E) as functions of centrosome separation.

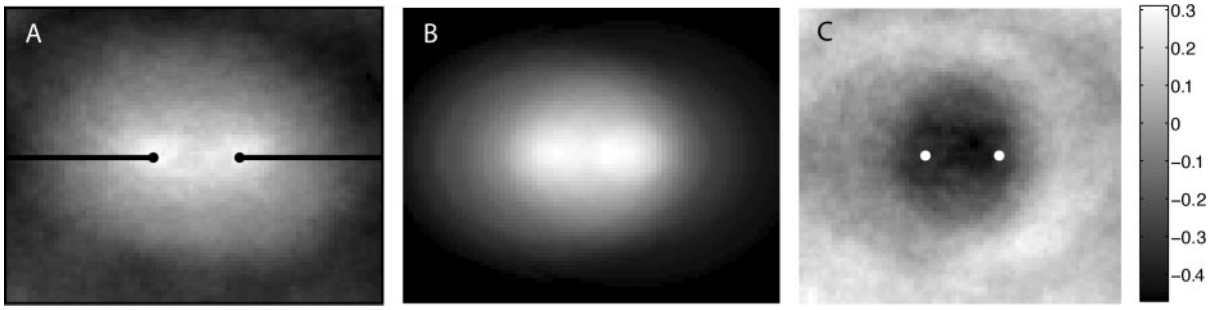

Figure 8. Experimental verification of the asymmetry of MT asters. The tubulin signals from individual spindles from time-lapse movies of GFP-tubulin embryos were digitally extracted, aligned so that the centrosome axis of all spindles was horizontal, grouped by centrosome distance, and, finally, averaged. Shown in A is one sample of the average tubulin signal from 75 spindles with centrosomes 2.0 ± 0.1 μm apart taken from two embryos. (B) The theoretical superposition of the signals from two asters one would expect if the MTs from each centrosome were distributed in a radially symmetric manner. (C) Difference between the average tubulin signal in A and the symmetric superposition signal in B. The shadow bar gives a measure of relative tubulin density in C; negative values correspond to MT depletion.

To determine whether elongation of the nucleus increases with centrosome separation, a linear regression of the elongation data were carried out (our unpublished data). The slope of this regression line was 0.13, indicating a slight increase in nuclear elongation as the centrosomes separate. Note that up until the pole-to-pole distance reaches the size of the nuclear diameter, one would not expect to see any deformation but beyond that point deformation should occur. Separating the data into two sections according to this expectation, we find that early during separation, elongation is essentially uncorrelated (slope of −0.02) with pole-to-pole distance, whereas after the centrosomes reach the edges of the nucleus, the slope increases to 0.5.

Note that the nuclear deformation is small and usually not apparent to the naked eye. Macroscopically, the intercentrosome distance would be in exact alignment with the long axis of the deformed nucleus, but in the microscopic environment of the cell, thermal forces and internal nuclear movements deform the nucleus, stochastically making the alignment imperfect. Our measurements mean that thermal and internal nuclear deformations are of the same order of magnitude as the elastic deformations induced by the outward force of the separating centrosomes. The observed correlation means that the centrosome-induced deformation is not negligible.

To test for a correlation between elongation axis and centrosomal axis, we considered the distribution of angles between these two axes at different pole-to-pole distances. Statistical tests (see *Materials and Methods*) revealed that when the centrosomes are separated by a distance <80% of the diameter of the nucleus, the distributions of angles cannot be distinguished from a uniform distribution but above 80%, we can reject the hypothesis that the distributions are uniform. A scatter plot of the data points is shown in Figure 7E. The tapering of the scatter plot seen as centrosome distance exceeds 80% of the size of the nucleus illustrates that the elongation and centrosome axes align late in prophase.

Summarizing the results, it can be concluded that when paired centrosomes are relatively close together, the associated nucleus is not excessively deformed, and if there is any deformation, the direction of elongation is independent of the positions of the centrosomes. As the centrosomes reach opposite sides of the nucleus, any nuclear elongation that we can detect aligns with the direction of proposed pulling by the centrosomes, indicating that the nucleus is not rigid and that the deformation of the nucleus may apply forces to the separating spindle.

MT Asters Are Asymmetric, Depleted near the Spindle Equator

The dynein generated force depends on how many astral MTs reach the actin cortex, where they reach the cortex, and where dynein motors are located. Figure 8 shows three images that we used to investigate the astral MT distribution. In Figure 8A, we show the tubulin signal taken from a confocal plane below the cortex but above the centrosomes averaged over 75 (aligned) buds, each at the same stage of centrosome separation (2 μm apart, denoted by small black circles). This image can be interpreted as the probability distribution for subcortical tubulin, or the polymer density of the astral MTs in the developing spindle, in the sense that the intensity at a given pixel is proportional to the probability of finding tubulin in that pixel in a typical bud. A similar averaging has been used in the study of kinetochore positioning in yeast mitotic spindle (Sprague *et al.*, 2003). The two high-intensity regions correspond to the centrosomes, whereas at the edge of the image (roughly 3–4 μm away), tubulin intensity drops off significantly.

To test whether each of the two centrosome-anchored MT asters is radially symmetric about their respective centrosomes, we need to compare the actual tubulin distribution to a theoretically determined tubulin distribution from hypothetical symmetric asters (Figure 8B). To construct image B, we assume that the measured tubulin density distal to the centrosomes (that is, in the left and right thirds of image A) corresponds to the MT length density of a single aster emanating from the closest centrosome. This assumption is valid provided that the contributions to the tubulin density from a few very long MTs originated from the opposite centrosome are negligible and that there are no interactions between MTs from the two asters in the distal regions. We can think of a line scan through these distal regions (black lines) as being equivalent to radial scans through a single centrosome aster. Rotating these line scans about the two centrosomes and summing up the signal, we obtain Figure 8B, which represents a theoretical scenario in which the tubulin distribution corresponds to the superposition of two completely radially symmetric MT asters. Note that the total number of MTs originating from each centrosome is not

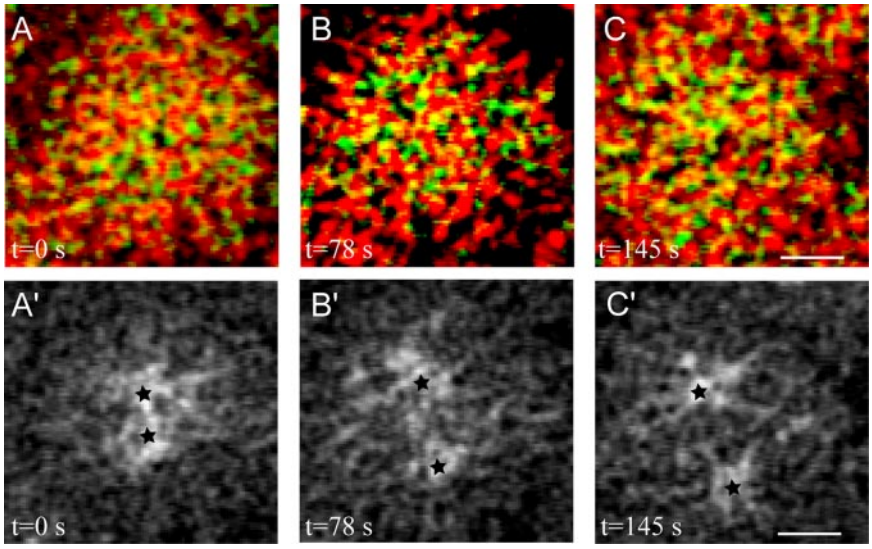

Figure 9. MTs and actin at the cortex. Snapshots (0, 78, and 145 s) of MTs (green) and actin (red) at the cortex (A-C) taken from live images of GFP-tubulin-expressing embryo injected with rhodamine-actin. Yellow area shows MTs contacting actin at the very cortex throughout the duration of early spindle morphogenesis. Stars in A′–C′ show the corresponding centrosomes position 2 μm below the cortex. Bars, 2 μm.

necessarily equal, so the two asters in Figure 8B are not quite identical. The tubulin density of this symmetric superposition is different from the measured tubulin density near the spindle equator, between the centrosomes. To detect this difference, we took the pointwise difference in intensities between images A and B in Figure 8, thereby generating image C. Notice that there is a pronounced dark region (corresponding to negative values) between the centrosomes in image C, indicating that the intensity in that region is lower in image A than in image B. This is indicative of "depletion" of MTs in the spindle equatorial region and hence of asymmetry of each aster. This result indicates that the number of MTs reaching the cortex near the spindle equator is less than that in the distal regions of the cortex, which supports the idea that MTs interacting with dynein at the cortex generate a net outward force.

We also observed significant tubulin–actin colocalization at the cortex throughout the mitotic cycle (Figure 9), lending further support to the idea that astral MTs can both mediate actin dynamics regulation, and contact dynein motors at the cortex to develop outward force.

Quantitative Force Balance Model of the Spindle

To properly understand the mechanisms of spindle morphogenesis, it is informative to quantify the movement of the major players in the process, but it would be even more valuable to determine the forces that underlie these movements. It is difficult to implement direct and invasive biophysical techniques in vivo; however, we use live and fixed fluorescent microscopy coupled with sophisticated data analysis techniques and quantitative modeling to estimate the relevant forces. First, we use a simple mathematical model to test the force balance in the developing spindle and then test the modeling hypotheses using realistic stochastic computations.

Mathematical Model. As a simple model for centrosome separation, we derive a single equation for $S(t)$, the distance between the centrosomes as a function of time. The forces acting on the centrosomes include a constant outward dynein force; the force of the cross-linking motor Ncd; the nuclear elastic force; and, finally, the drag force (Figure 10A). Assuming linear force-velocity relations for dynein and Ncd motors (see *Materials and Methods*), the following one-dimensional force balance equation describes the time course of pole separation:

$$n_d F_d\left(1-\frac{1}{2v_d}\frac{dS}{dt}\right) = \rho_{ncd} S F_{ncd}\left(1+\frac{1}{2v_n}\frac{dS}{dt}\right) + F_{nucl}(S) + \frac{\mu}{2}\frac{dS}{dt} \quad (1)$$

outward dynein force | inward Ncd force | inward nuclear elastic force | effective viscous drag

where n_d is the number of active dynein motors pulling outward on the centrosomes; ρ_{ncd} is the number of Ncd motors per micron of ipMT overlap; F_d and F_{ncd} are the dynein and Ncd stall forces, and v_d and v_n are the corresponding unloaded velocities; and μ is the effective drag coefficient for the centrosomes. All parameter values are specified in Table S1. At separation greater than the nuclear diameter, D, the nuclear elastic force can be approximated by a linear spring (see *Materials and Methods*): $F_{nucl}(S) \approx k(S - D)$, where k is the effective nuclear spring constant. From Eq. 1, we can extract an estimate for the prophase steady-state separation ($dS/dt = 0$):

$$S_{st} = \frac{n_d F_d + kD}{\rho_{ncd} F_{ncd} + k} \quad (2)$$

Linearizing Eq. 1 near the steady state, it is easy to find that $S(t) \sim S_{st}(1 - \exp[-t/\tau])$ and to estimate the time constant for the pre-NEB separation of the centrosomes:

$$\tau = \frac{\frac{n_d F_d}{2v_d} + \frac{\rho_{ncd} F_{ncd} S_{st}}{2v_n} + \frac{\mu}{2}}{\rho_{ncd} F_{ncd} + k} \quad (3)$$

To analyze large data sets from several embryos and to improve the statistics of the data collected, we fit each individual separation time course with a simple two-parameter fit (a logistic function) to find values of S_{st} and τ for each spindle. This permits us to calculate not only the mean steady state and time constant but also the variation in these as well. Figure 3 shows the accumulated data through cycles 11, 12, and 13. We found that the wild-type and Ncd null steady states and time constants are statistically indistinguishable in cycles 11 and 12. In cycle 13, the steady-state

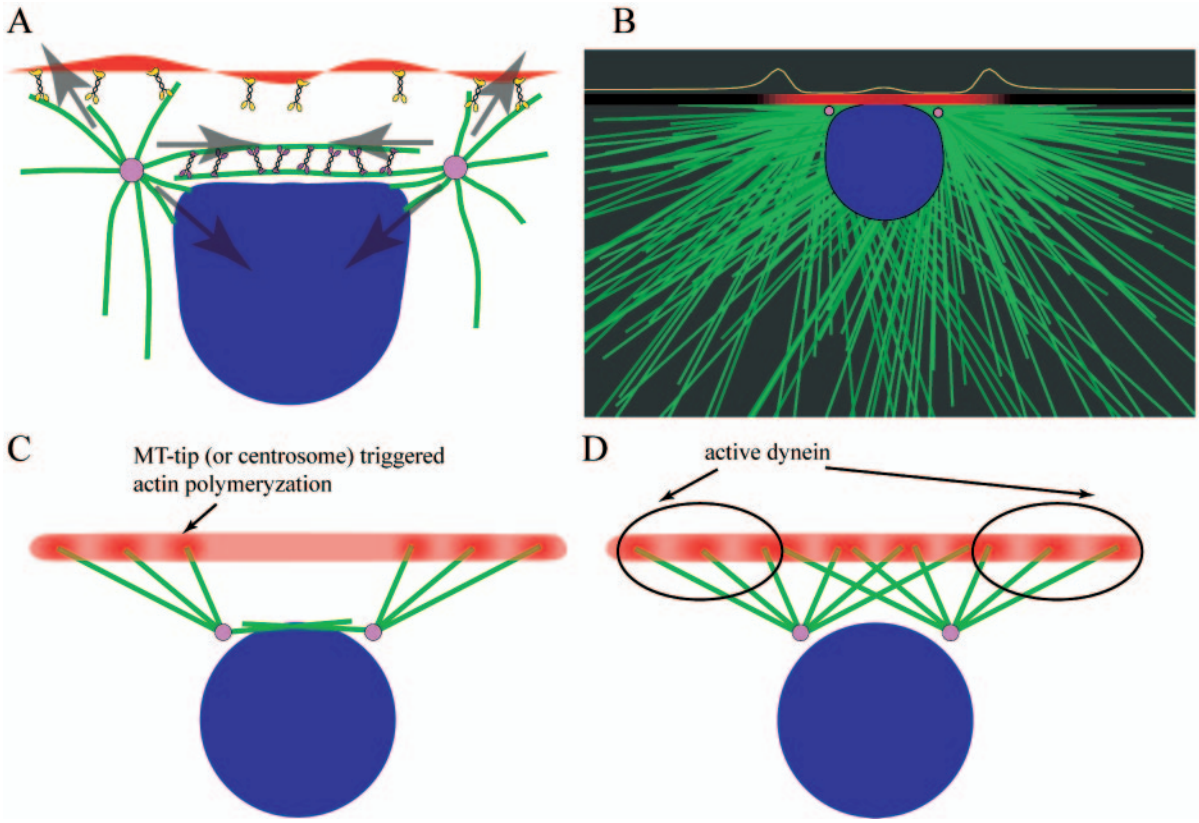

Figure 10. (A) Proposed model of spindle morphogenesis. The centrosomes separate to the prophase steady state determined by the balance of a constant outward dynein force and the sum of the inward Ncd force and nuclear elastic force. (B) Snapshot of the computer simulation. The yellow curve above shows the predicted level of dynein activation. The red shading of the cortex indicates the predicted graded actin density (bright, high density; dark, low density). Note that the nucleus is deformed and pressed against the actin cortex. (C) Hypothesis I: Depletion of "inner" astral MTs decreases the inward dynein force on centrosomes but increases the inward Ncd force. However, short ipMT bundles limit the Ncd force when the centrosomes are close, but, as centrosomes separate, the Ncd force grows to match the outward force generated by dynein at the cortex. (D) Hypothesis II: MT tips locally inhibit dynein at the cortex. In the vicinity of the centrosomes and at the spindle equator, MT tips from both poles overlap, so there is a high effective density of MT tips, and dynein is inhibited. In the regions distal to the centrosomes, MT tips from only one pole reach the cortex, so there is a low effective density of MT tips, and dynein is active. Note that dynein is active where it can generate the outward forces.

separation is significantly larger in the Ncd null embryo than in the wild-type embryo, as reported previously (Sharp *et al*. 2000a), and the separation takes significantly longer in wild type than in Ncd null but the Ncd null time constant does not differ significantly from the previous two cycles.

The model depends on nine parameters: F_d, F_{ncd}, v_d, v_n, D, k, ρ_{ncd}, μ, and n_d. The orders of magnitude of the first four of them are available from the literature (Table S1). We measure the nuclear diameter in this work and estimate the spring constant of the nucleus in *Materials and Methods* using available data. By measuring the prophase steady state and time constant in cycles 11, 12, and 13 in Ncd null embryos and using the described fitting procedure, we estimate parameters n_d and μ (Table 2). Then, using the fitting results for the wild-type embryos, we estimate ρ_{ncd} (Table 2).

Note, that the estimated number of Ncd motors per micrometer is compatible with the motor's size (20–30/μm). Also, the estimated number of active and pulling dynein motors (10–30) compares well with independent estimates (Grill *et al*., 2003). Note also that the viscous drag coefficient of the MT aster is of the order of hundreds of piconewtons·second per micrometer. The effective viscous drag from nuclear deformation can be estimated from the existing data (Tseng *et al*., 2004) to have the same order of magnitude. From fitting our data, we estimate the full effective viscous drag to be 1 order of magnitude greater, which most likely indicates sources of friction other than the fluid of the cytosol.

Computational Model. Although the simple mathematical model realistically describes the separation time course, it assumes the existence of an asymmetry in the distribution of dynein motors pulling on astral MTs and reduces the system

Table 2. Model parameters estimated in this study

	Cycle 11	Cycle 12	Cycle 13
n_d (number of working dynein motors per centrosome)	28 (140)	21 (105)	14 (70)
ρ_{ncd} (number of working Ncd motors per micrometer)	0	0	26
μ (effective centrosome drag coefficient, piconewtons·second per micrometer)	5.10^3	7.10^3	8.10^3

to a single dimension that is the axis between the centrosomes. This oversimplifies the system and ignores the stochastic aspects of pole separation. To model spindle morphogenesis on a more realistic level, we generalized the force balance equation described above to a higher dimension. Although a three-dimensional generalization of this model is simple to formulate, it would be a technical and computationally intensive improvement but not necessarily informative so we restrict ourselves to a two-dimensional cross-sectional model. In the computational model, we use Monte Carlo calculations to simulate MT asters undergoing dynamic instability, pushing against the cortex by polymerization, pulling on the cortex via dynein, and undergoing dynamic cross-linking and contraction mediated by Ncd (Videos 3 and 4). In addition, we treat the nucleus as an elastic body. The details are described in *Materials and Methods*. A snapshot from the computer simulations is shown in Figure 10B.

Most importantly, the model allows us to investigate the hypothetic mechanisms of the outward dynein force generation. In our previous work (Cytrynbaum *et al*., 2003), we assumed that the corresponding asymmetry in dynein-generated forces was due to nonuniformities of the actin cap: hollow on top with furrows surrounding the nascent spindle. Data presented in this article indicate that this geometry is incorrect and other sources of asymmetry are required. We propose two possibilities: 1) depletion of astral MTs from the inner spindle region by cross-linking (Figure 10C) and 2) centrosome- or MT-based regulation of dynein (Figure 10D).

The first mechanism causes depletion of the astral MTs from the region between the spindle poles, because in that region MTs from opposite centrosomes can intersect and get cross linked into the ipMT bundle by Ncd or other MAPs. Then, only MTs growing outward reach the cortex, which leads to the outward pulling force asymmetry (Figure 10C). Thus, there is a loss of inward force at the cortex but a gain of inward force by Ncd. Despite this apparently compensating gain, separation is nonetheless facilitated by this transfer of MTs from the cortex to ipMT bundles; when centrosomes are close together, the length of ipMT bundles is limited to the distance between centrosomes thereby keeping the force produced by Ncd to a minimum. Thus, the loss of inward force generated by cortical MTs is greater than the gain in inward force by Ncd, allowing the centrosomes to move apart. As the centrosomes separate, the length of the ipMT bundles increases leading to an increase in the Ncd and nuclear elastic forces until the outward force generated by cortical MTs balances the inward force and the centrosomes come to rest at a steady distance. One difficulty with this MT depletion mechanism is that in Ncd null embryos, there might be less cross-linking and hence less cortical depletion of MTs. However, it is possible that other cross-linkers are involved, especially considering that Ncd is nonprocessive and hence unlikely to be the sole cross-linker.

The second mechanism requires the presence of a kinase or other regulatory molecule (diffusing in the cytoplasm or being transported on the astral MTs) that is activated at the centrosomes, deactivated in the cytosol, and, when active, down-regulates dynein at the cortex. This means that there is a region around each centrosome from which neither centrosome is pulled. This does not generate asymmetry for a single centrosome but with two centrosomes present, each one feels a weaker cortical pull toward the other than away from the other (Figures 10, B and D). Indeed, in the vicinity of the centrosomes and at the spindle equator, MT tips from both poles overlap, so there is a high effective density of MT tips, more regulatory molecules are delivered, and dynein is inhibited. In the regions distal to the centrosomes, MT tips from only one pole reach the cortex, so there is a low effective density of MT tips, less regulatory molecules are delivered, and dynein is active. Note that dynein is active where it can generate the outward forces. Diffusion from the centrosomes through the cytoplasm causes the same effect. Computer simulations (see *Materials and Methods*) show that either of these mechanisms, or their combination is sufficient to generate the necessary outward asymmetry of the dynein force.

The simulations also confirmed that the detailed force balance keeps the centrosomes separating along the linear trajectories right under the cortex and that the nucleus is "squashed" against the cortex. The simulations revealed significant stochastic fluctuations in the separation rates and asymmetries between the sister centrosomes in agreement with our experimental observations. These fluctuations and asymmetry are due to significant fluctuations in the number of astral MTs reaching the cortex and developing the pulling force (their number oscillates ~30%).

Finally, we simulated the F-actin cap dynamics. It has been suggested that the dynamic redistribution of actin is due to transport of actin along MTs by an unidentified plus end directed motor (Foe *et al*., 2000), one possible candidate being Pav-KLP (Minestrini *et al*., 2003). One possible problem with this mechanism is the previously described 'hollowing out' of the actin caps (Foe *et al*., 2000), which is not supported by our observations. Instead, we suggest a polymerization/depolymerization mechanism mediated by e.g., a kinase either diffusing from the centrosomes or being transported on the astral MTs. Evidence in favor of this hypothesis includes studies implicating Abelson kinase in actin regulation and furrow formation (Korey and Van Vactor, 2000; Grevengoed *et al*., 2003), localization of actin nucleating protein Arp2/3 to the edges of the expanding caps (Stevenson *et al*., 2002), and localization of plus-end directed motor Pav-KLP, which interacts with actin-regulating proteins, to the furrows and cap edges (Minestrini *et al*., 2003). We used the model to simulate the kinase distribution and resulting F-actin dynamics (see *Materials and Methods*). The model predicts the F-actin cap expanding (Figure 10B) synchronously with the separating centrosomes provided the actin polymerization/depolymerization kinetics, as well as the kinase dynamics are at least a few fold faster than the characteristic rate of centrosome separation.

DISCUSSION

Over the last few years, much has been learned about the role of individual motors in cytoskeletal organization during mitosis (Goshima and Vale, 2003; Kwon and Scholey, 2004). However, despite available molecular information, the task of constructing a mechanistic and quantitative understanding of mitosis remains a major challenge. Following several recent studies (Sprague *et al*., 2003; Brust-Mascher *et al*., 2004), we used a combination of experimental and modeling tools to understand the coordinated behavior of motors, MTs, actin, and the nucleus in spindle morphogenesis.

Quantitative data gathered from observations of successive cycles in the syncytial blastoderm stage of the *Drosophila* early embryo combined with modeling allows us to conclude that the nucleus plays a crucial role in determining the size of the nascent spindle at the end of prophase. In addition, we observe that the nucleus deforms and aligns with the spindle axis, so we suggest that nuclear elasticity (assisted by Ncd in cycle 13) develops a spring-like inward

force growing with the pole-to-pole separation. We provide evidence that dynein is spread more or less uniformly throughout the actin cortex, in the shape of solid and flat, not hollowed out, caps expanding in synchrony with the separating centrosomes. Interestingly, cap expansion is not accompanied by furrow ingression during the pre-NEB stage. Moreover, the subcortical linear trajectories of the centrosomes imply an outward force on the spindle originating at the cortex.

Comparing successive cycles in the blastoderm stage, we conclude that Ncd, which colocalizes with the ipMT bundles, does not play as significant a role in pre-NEB centrosome separation before cycle 13 as it does in cycle 13 (the cycle studied in Sharp *et al*. 2000a). This observation is consistent with the fact that it is only after cycle 12, when the cortex is crowded with hundreds of buds, that the embryo must implement additional means of preventing inappropriate MT–kinetochore connections between buds. It seems more likely that NCD affects the final spindle length rather than the centrosomes' ability to separate or their separation rate. For example, it could be that Ncd is one of the cross-linking agents responsible for ipMT bundling and thus it indirectly regulates the outward force acting on the spindle poles. Also, Ncd action could be ipMT-length dependent due to plausible collective motor effects. To conclude, Ncd is probably not essential during spindle assembly and nuclear elasticity is in fact equally or more important in determining spindle size, particularly in the Ncd-null embryo.

Our computational model leads us to suggest that the actin cap growth at the cortex is regulated by the centrosomes with possible involvement of astral MTs, and that dynein at the cortex generates a constant outward force. Of course, other structures in the vicinity of the centrosomes, such as the nucleus, are alternative candidate sources of kinases generating the diffusible signal. The model predicts that to generate sufficient outward force, either dynein activity has to be locally inhibited by the centrosomes, or astral MTs have to be depleted at the cortex between the centrosomes by cross-linking or other mechanisms, or both; otherwise, the dynein force would have a significant inward component, and pole separation could not proceed. The simplest interpretation of our results is that cap expansion is directly affected by centrosome- or astral-MT-mediated regulation of actin. Furthermore, actin polymerization dynamics has to be at least as fast as centrosome separation, or otherwise, actin cap growth would be rate limiting and centrosomes would not be able to move any faster in the Ncd null embryo than in wild type.

On a more quantitative front, the computational model predicts that the total dynein force is of the order of tens of piconewtons, indicating that tens of dynein motors at the cortex function by pulling on tens of astral MTs. This is in agreement with previously estimated numbers of MTs (Piehl and Cassimeris, 2003) and of pulling dynein motors (Grill *et al*., 2003) in other cells. Following Cytrynbaum *et al*. (2003), we predict an unexpectedly large value of the effective viscous drag coefficient of the centrosome. One plausible explanation is a dynamic cross-linking of astral MTs to either the nuclear envelope, F-actin, or the hypothetical spindle matrix. Alternatively, motor-mediated sliding may have effective friction associated with it. Also, in contrast with our earlier modeling attempts, the time series for pole separation can be fit without the MT polymerization force that we invoked in the initial model (Cytrynbaum *et al*., 2003). There is no convincing proof, however, that this force does not contribute to spindle morphogenesis; future research is needed to resolve this issue.

To summarize, we have significantly improved the previous spindle elongation model (Sharp *et al*., 2000a; Cytrynbaum *et al*., 2003) by resolving existing uncertainties and proposing new hypotheses. The resulting quantitative model successfully explains the obtained data, including the kinetics of pole separation before NEB, through the balance of effective drag, dynein, and nuclear elastic forces and of the Ncd force in cycle 13.

Our updated model underscores additional uncertainties that should be addressed in future studies. For example, cortical myosin II was identified as a critical motor for spindle assembly in some cells (Rosenblatt *et al*., 2004). However, we feel it is unlikely to play an important role in the interphase–prophase force-balance analyzed in our studies 1) based on direct observations of syncytial embryos (Foe *et al*., 2000; Royou *et al*., 2004); 2) because myosin II was found to act only after NEB (Rosenblatt *et al*., 2004), which is not relevant to our studies addressing pre-NEB spindle assembly; and 3) because the suggested coordinated cortical expansion and contraction model (Rosenblatt *et al*., 2004) seems to require a circumferential cortex surrounding the entire spindle, which is also not relevant to the syncytial blastoderm where the cortex is adjacent to only one surface of the spindle. Given the conservation of spindle-associated force-generating mechanisms, however, directly testing the role of actin-myosin II sliding in the force balance will be worthwhile. In addition, rapid motor-mediated transport of regulatory molecules along astral MTs may influence the growth of the actin cap edges and the activity of cortical dynein, Pav-KLP being one candidate (Minestrini *et al*., 2003), but other mechanisms, including transport of F-actin and MT cross-linking, are also possible. Specifying the nature of such mechanisms is of utmost importance. Measurements of MT nucleation and dynamic instability parameters are needed to verify the model assumptions. It would be very important to obtain a spatial-temporal map of dynein activity. Direct biophysical measurements of the nuclear mechanics as well as the numbers, force-velocity relationships and collective force-generating properties of the multiple molecular motors would make our understanding of spindle morphogenesis more precise. Another open biophysical question is the nature and magnitude of the effective viscous drag on the centrosomes. The crowding effects of the synchronous division of thousands of nuclei near the embryo's surface have not yet been explored and will likely uncover interesting interbud interactions. Finally, extending the quantitative model to describe later stages of mitosis, a process already begun in (Brust-Mascher *et al*., 2004), is necessary for understanding the role of forces and movements in spindle morphogenesis.

Our work also seems to be relevant to the currently intriguing question of whether the mitotic spindle contains an additional mechanical component, the spindle matrix, whose activity augments those of microtubules and mitotic motors in driving spindle morphogenesis and chromosome motility (Scholey *et al*., 2001; Wells, 2001; Bloom, 2002). Although no definitive evidence for the existence of such a matrix exists, proposed candidates include actin, NuMA/Asp, the elastic "microtrabecular matrix" (reviewed in Scholey *et al*., 2001) the *Drosophila* skeletor–megator–chromator matrix (Walker *et al*., 2000; Qi *et al*., 2004) and poly-(ADP-ribose) (Chang *et al*., 2004). In our initial model for early spindle morphogenesis (Cytrynbaum *et al*., 2003), we argued that such a spindle matrix is not required because a force-balance involving only MT polymer ratchets, mitotic motors, and the cortex could account for the dynamics of spindle pole separation. However, it could be argued that

the augmentation of the force-generating properties of MTs and motors by cortical and nuclear dynamics fulfills some of the functions proposed for the matrix. Indeed, in some respects the inward elastic restoring force exerted by nuclear deformation on the spindle poles acts in the manner proposed for the hypothetical elastic microtrabecular matrix. It will therefore be interesting to determine whether this mechanical function of the nucleus in spindle morphogenesis is transferred to another spindle component such as the skeletor–megator–chromator complex after NEB at which times the nuclear envelope cannot serve as an underlying mechanical substrate.

Our findings have general cell biological implications, because many crucial phenomena suggest self-organizing interactions between microtubules, actin, and molecular motors. These include maintaining the polarity of migrating cells and the formation of a contractile ring and cleavage furrow in cytokinesis (reviewed in Rodriguez *et al*., 2003). An important feature of all such interactions is cross-talk between mechanical and force- and movement-generating molecular machines and biochemical regulation mechanisms. In this study, MTs, the nucleus, and dynein and Ncd motors play the role of the former, whereas our proposed actin and dynein regulators, potentially delivered by MT-mediated pathways, play the role of the latter. A combination of experimental studies and quantitative modeling of such complex mechanochemical machines proved to be very effective in recent studies of the mitotic spindle (Grill *et al*., 2003; Sprague *et al*., 2003; Brust-Mascher *et al*., 2004); our article is another step down this road.

ACKNOWLEDGMENTS

We thank R. Ananthakrishnan, R. Wollman, D. Cheerambathur, M. F. Tsou, G. Odell, and V. Foe for useful suggestions. We are supported by national Institutes of Health Grants GM-55507 and GM-068952. E.N.C. was funded by the Burroughs Welcome Fund through the Program in Mathematics and Molecular Biology.

REFERENCES

Bloom, K. (2002). Yeast weighs in on the elusive spindle matrix: new filaments in the nucleus. Proc. Natl. Acad. Sci. USA *99*, 4757–4759.

Brust-Mascher, I., Civelekoglu-Scholey, G., Kwon, M., Mogilner, A., and Scholey, J. M. (2004). Model for anaphase B: role of three mitotic motors in a switch from poleward flux to spindle elongation. Proc. Natl. Acad. Sci. USA *101*, 15938–15943.

Chang, P., Jacobson, M. K., and Mitchison, T. J. (2004). Poly(ADP-ribose) is required for spindle assembly and structure. Nature *432*, 645–649.

Cytrynbaum, E. N., Scholey, J. M., and Mogilner, A. (2003). A force balance model of early spindle pole separation in Drosophila embryos. Biophys. J. *84*, 757–769.

Dahl, K. N., Kahn, S. M., Wilson, K. L., and Discher, D. E. (2004). The nuclear envelope lamina network has elasticity and a compressibility limit suggestive of a molecular shock absorber. J. Cell Sci. *117*, 4779–4786.

Dogterom, M., and Leibler, S. (1993). Physical aspects of the growth and regulation of microtubule structures. Phys. Rev. Lett. *70*, 1347–1350.

Dogterom, M., and Yurke, B. (1997). Measurement of the force-velocity relation for growing microtubules. Science. *278*, 856–860.

Dujardin, D. L., and Vallee, R. B. (2002). Dynein at the cortex. Curr. Opin. Cell Biol. *14*, 44–49.

Foe, V. E., and Alberts, B. M. (1983). Studies of nuclear and cytoplasmic behaviour during the five mitotic cycles that precede gastrulation in *Drosophila* embryogenesis. J. Cell Sci. *61*, 31–70.

Foe, V. E., Field, C. M., and Odell, G. M. (2000). Microtubules and mitotic cycle phase modulate spatiotemporal distributions of F-actin and myosin II in *Drosophila* syncytial blastoderm embryos. Development *127*, 1767–1787.

Goshima, G., and Vale, R. D. (2003). The roles of microtubule-based motor proteins in mitosis: comprehensive RNAi analysis in the *Drosophila* S2 cell line. J. Cell Biol. *162*, 1003–1016.

Grevengoed, E. E., Fox, D. T., Gates, J., and Peifer, M. (2003). Balancing different types of actin polymerization at distinct sites: roles for Abelson kinase and Enabled. J. Cell Biol. *163*, 1267–1279.

Grill, S. W., Howard, J., Schaffer, E., Stelzer, E. H., and Hyman, A. A. (2003). The distribution of active force generators controls mitotic spindle position. Science *301*, 518–521.

Hirakawa, E., Higuchi, H., and Toyoshima, Y. Y. (2000). Processive movement of single 22S dynein molecules occurs only at low ATP concentrations. Proc. Natl. Acad. Sci. USA *97*, 2533–2537.

Houchmandzadeh, B., Marko, J. F., Chatenay, D., and Libchaber, A. (1997). Elasticity and structure of eukaryote chromosomes studied by micromanipulation and micropipette aspiration. J. Cell Biol. *139*, 1–12.

Inoue, S., and Salmon, E. D. (1995). Force generation by microtubule assembly/disassembly in mitosis and related movements. Mol. Biol. Cell *6*, 1619–1640.

Kapitein, L. C., Peterman, E. J., Kwok, B. H., Kim, J. H., Kapoor, T. M., and Schmidt, C. F. (2005). The bipolar mitotic kinesin Eg5 moves on both microtubules that it crosslinks. Nature. *435*, 114–118.

Karabay, A., and Walker, R. A. (1999). Identification of microtubule binding sites in the Ncd tail domain. Biochemistry *38*, 1838–1849.

Karr, T. L., and Alberts, B. M. (1986). Organization of the cytoskeleton in early *Drosophila* embryos. J. Cell Biol. *102*, 1494–1509.

Kellogg, D. R., Mitchison, T. J., and Alberts, B. M. (1988). Behaviour of microtubules and actin filaments in living *Drosophila* embryos. Development. *103*, 675–686.

Korey, C. A., and Van Vactor, D. (2000). From the growth cone surface to the cytoskeleton: one journey, many paths. J. Neurobiol. *44*, 184–193.

Kwon, M., and Scholey, J. M. (2004). Spindle mechanics and dynamics during mitosis in *Drosophila*. Trends Cell Biol. *14*, 194–205.

Lawrence, C. J., *et al*. (2004). A standardized kinesin nomenclature. J. Cell Biol. *167*, 19–22.

Marshall, W. F., Marko, J. F., Agard, D. A., and Sedat, J. W. (2001). Chromosome elasticity and mitotic polar ejection force measured in living *Drosophila* embryos by four-dimensional microscopy-based motion analysis. Curr. Biol. *11*, 569–578.

McDonald, H. B., Stewart, R. J., and Goldstein, L. S. (1990). The kinesin-like Ncd protein of *Drosophila* is a minus end-directed microtubule motor. Cell *63*, 1159–1165.

McIntosh, J. R., Hepler, P. K., and Van Wie, D. G. (1969). Models for mitosis. Nature *224*, 659–663.

Minestrini, G., Harley, A. S., and Glover, D. M. (2003). Localization of Pavarotti-KLP in living *Drosophila* embryos suggests roles in reorganizing the cortical cytoskeleton during the mitotic cycle. Mol. Biol. Cell *14*, 4028–4038.

Nedelec, F. (2002). Computer simulations reveal motor properties generating stable antiparallel microtubule interactions. J. Cell Biol. *158*, 1005–1015.

Nishida, E., Iida, K., Yonezawa, N., Koyasu, S., Yahara, I., and Sakai, H. (1987). Cofilin is a component of intranuclear and cytoplasmic actin rods induced in cultured cells. Proc. Natl. Acad. Sci. USA *84*, 5262–5266.

Piehl, M., and Cassimeris, L. (2003). Organization and dynamics of growing microtubule plus ends during early mitosis. Mol. Biol. Cell *14*, 916–925.

Qi, H., Rath, U., Wang, D., Xu, Y. Z., Ding, Y., Zhang, W., Blacketer, M. J., Paddy, M. R., Girton, J., Johansen, J., and Johansen, K. M. (2004). Megator, an essential coiled-coil protein that localizes to the putative spindle matrix during mitosis in *Drosophila*. Mol. Biol. Cell *15*, 4854–4865.

Robinson, J. T., Wojcik, E. J., Sanders, M. A., McGrail, M., and Hays, T. S. (1999). Cytoplasmic dynein is required for the nuclear attachment and migration of centrosomes during mitosis in *Drosophila*. J. Cell Biol. *146*, 597–608.

Rodriguez, O. C., Schaefer, A. W., Mandato, C. A., Forscher, P., Bement, W. M., and Waterman-Storer, C. M. (2003). Conserved microtubule-actin interactions in cell movement and morphogenesis. Nat. Cell Biol. *5*, 599–609.

Rosenblatt, J., Cramer, L. P., Baum, B., and McGee, K. M. (2004). Myosin II-dependent cortical movement is required for centrosome separation and positioning during mitotic spindle assembly. Cell *117*, 361–372.

Royou, A., Field, C., Sisson, J. C., Sullivan, W., and Karess, R. (2004). Reassessing the role and dynamics of nonmuscle myosin II during furrow formation in early *Drosophila* embryos. Mol. Biol. Cell *15*, 838–850.

Scholey, J. M., Brust-Mascher, I., and Mogilner, A. (2003). Cell division. Nature. *422*, 746–752.

Scholey, J. M., Rogers, G. C., and Sharp, D. J. (2001). Mitosis, microtubules, and the matrix. J. Cell Biol. *154*, 261–266.

Sharp, D. J., Brown, H. M., Kwon, M., Rogers, G. C., Holland, G., and Scholey, J. M. (2000a). Functional coordination of three mitotic motors in Drosophila embryos. Mol. Biol. Cell *11*, 241–253.

Sharp, D. J., McDonald, K. L., Brown, H. M., Matthies, H. J., Walczak, C., Vale, R. D., Mitchison, T. J., and Scholey, J. M. (1999a). The bipolar kinesin, KLP61F, cross-links microtubules within interpolar microtubule bundles of *Drosophila* embryonic mitotic spindles. J. Cell Biol. *144*, 125–138.

Sharp, D. J., Rogers, G. C., and Scholey, J. M. (2000b). Cytoplasmic dynein is required for poleward chromosome movement during mitosis in *Drosophila* embryos. Nat. Cell Biol. *2*, 922–930.

Sharp, D. J., Yu, K. R., Sisson, J. C., Sullivan, W., and Scholey, J. M. (1999b). Antagonistic microtubule-sliding motors position mitotic centrosomes in Drosophila early embryos. Nat. Cell Biol. *1*, 51–54.

Sprague, B. L., Pearson, C. G., Maddox, P. S., Bloom, K. S., Salmon, E. D., and Odde, D. J. (2003). Mechanisms of microtubule-based kinetochore positioning in the yeast metaphase spindle. Biophys J. *84*, 3529–3546.

Stevenson, V., Hudson, A., Cooley, L., and Theurkauf, W. E. (2002). Arp2/3-dependent pseudocleavage [correction of psuedocleavage] furrow assembly in syncytial *Drosophila* embryos. Curr. Biol. *12*, 705–711.

Stevenson, V. A., Kramer, J., Kuhn, J., and Theurkauf, W. E. (2001). Centrosomes and the Scrambled protein coordinate microtubule-independent actin reorganization. Nat. Cell Biol. *3*, 68–75.

Sullivan, W., and Theurkauf, W. E. (1995). The cytoskeleton and morphogenesis of the early *Drosophila* embryo. Curr. Opin. Cell Biol. *7*, 18–22.

Tram, U., Riggs, B., and Sullivan, W. (2001). Cleavage and gastrulation in *Drosophila* embryos. Macmillan Reference Ltd. *In* Encyclopedia of Life Sciences, London: Nature Publishing Group, 1–7.

Tseng, Y., Lee, J. S., Kole, T. P., Jiang, I., and Wirtz, D. (2004). Micro-organization and visco-elasticity of the interphase nucleus revealed by particle nanotracking. J. Cell Sci. *117*, 2159–2167.

Walker, D. L., Wang, D., Jin, Y., Rath, U., Wang, Y., Johansen, J., and Johansen, K. M. (2000). Skeletor, a novel chromosomal protein that redistributes during mitosis provides evidence for the formation of a spindle matrix. J. Cell Biol. *151*, 1401–1412.

Wells, W. A. (2001). Searching for a spindle matrix. J. Cell Biol. *154*, 1102–1104.